Magnetic Resonance Imaging 117 (2025) 110333

Contents lists available at ScienceDirect

Magnetic Resonance Imaging

journal homepage: www.elsevier.com/locate/mri

Improving MRI turbulence quantification by addressing the measurement errors caused by the derivatives of the turbulent velocity field – Sequence development and in-vitro validation

Swantje Romig [a,*], Kristine John [a], Simon Schmidt [b,c], Sebastian Schmitter [d], Sven Grundmann [a], Martin Bruschewski [a]

[a] Institute of Fluid Mechanics, University of Rostock, Rostock, Germany
[b] University of Minnesota (Center for Magnetic Resonance Research), Minneapolis, MN, United States of America
[c] Medical Physics in Radiology, German Cancer Research Center (DKFZ), Heidelberg, Germany
[d] Physikalisch-Technische Bundesanstalt (PTB), Berlin, Germany

ARTICLE INFO

Keywords:
Turbulence quantification
Phase contrast MRI
Intra-voxel phase dispersion
Reynold stress tensor
Turbulence kinetic energy

ABSTRACT

Purpose: To improve the current method for MRI turbulence quantification which is the intravoxel phase dispersion (IVPD) method. Turbulence is commonly characterized by the Reynolds stress tensor (RST) which describes the velocity covariance matrix. A major source for systematic errors in MRI is the sequence's sensitivity to the variance of the derivatives of velocity, such as the acceleration variance, which can lead to a substantial measurement bias.

Methods: We developed a Cartesian phase contrast sequence with FAST velocity encoding and two separately measured partial echoes with opposite readout directions. This design aims to reduce the high-order gradient moments that are responsible for the described measurement error. Velocity encoding directions follow the ICOSA6 scheme to capture the full RST. Turbulence data is reconstructed using the intra-voxel phase dispersion (IVPD) technique. We validated this sequence in vitro using a periodic hill flow benchmark with highly anisotropic turbulence. MRI data underwent extensive averaging, with multiple velocity encoding values employed to reduce noise and isolate systematic effects.

Results: The RST data obtained from the new sequence agree well with the ground truth. Compared to a state-of-the-art sequence, the maximum errors were reduced by factor five.

Conclusion: Simple adjustments to current MRI protocols can greatly enhance turbulence measurement accuracy through the reduction of high-order gradient moments. The proposed measures include applying FAST velocity encoding, high readout bandwidth, and a highly asymmetric readout. Ringing artifacts due to the asymmetric readout can be removed via a second, inverted readout.

1. Introduction

MRI recently gained more attention as a means to measure flow quantities in turbulent flows. Apart from the mean flow velocity, more advanced flow parameters for turbulence quantification, like the Reynolds stress tensor (RST), can be obtained using MRI. The RST describes the velocity covariance matrix including three normal and three shear stresses. An important turbulence parameter derived from the normal stresses as half the trace of the RST is the turbulence kinetic energy (TKE).

Measuring turbulence statistics is useful in a wide range of fields. TKE quantification is applied as a tool in clinical applications, where elevated levels of TKE are used for diagnostic purposes [1,2]. Current research focuses on in-vivo RST measurements in aortic flows [3–5]. However, MRI RST measurements are also performed in engineering applications to optimize energy efficiency in a refrigerator machine room [6], to measure gas flow in packed beds of non-spherical pellets used in the chemical process industry [7] or to measure transport processes through porous media occurring in heat transfer, chemical reactions or separation processes [8]. So, the same methods first

* Corresponding author.
E-mail address: swantje.romig@uni-rostock.de (S. Romig).

https://doi.org/10.1016/j.mri.2025.110333
Received 5 August 2024; Received in revised form 21 January 2025; Accepted 22 January 2025
Available online 23 January 2025
0730-725X/© 2025 The Authors. Published by Elsevier Inc. This is an open access article under the CC BY license (http://creativecommons.org/licenses/by/4.0/).

developed for medical applications are now also applied in an engineering context.

The first attempts to quantify turbulence using MRI applied Fourier velocity encoding (FVE), which samples the whole velocity spectrum within a voxel [9–11]. The current state-of-the-art approach for quantifying turbulence is based on intra-voxel phase dispersion (IVPD) using phase-contrast (PC) MRI methods, which is significantly faster than FVE. In the case of an intravoxel velocity distribution with finite width and the application of a non-zero first gradient moment M_1, the nuclear spins exhibit different velocity-dependent phases that add up incoherently, leading to signal attenuation. Hence, the components of the RST can be directly calculated from the relative signal magnitude; however, this deduction relies on certain underlying assumptions.

The velocity encoding time needs to be small compared to the turbulent time scales in the flow field [12,13]. This ensures that the velocity field is constant during the velocity encoding process. Moreover, the velocity distribution within the voxel is assumed to have a Gaussian shape and to be in the ergodic regime [13]. Based on these assumptions, Dyverfeldt et al. [14] derived a relationship between the signal magnitude from velocity-encoded MRI and the velocity standard deviation inside the voxel.

Dyverfeldt et al. [12] and Ha et al. [15] extended this encoding scheme to multiple velocity encoding steps per direction to increase the dynamic range of turbulence that can be acquired. They applied their method in medical contexts. Binter et al. followed a similar approach but used Bayesian analysis [16] [17]. They obtained a joint probability map for each encoding direction and voxel with the mean velocity on one axis and its standard deviation on the second axis. The location of the highest probability in the map leads to both mean velocity and its standard deviation.

On the engineering side of RST quantification, Elkins et al. [18] describe an extension to acquire individual shear stresses. These components of the RST can be calculated from the normal stresses in two directions and a further measurement with simultaneous velocity-sensitivity in both involved directions. Haraldsson et al. [19] acquired the whole RST using the ICOSA6 method, whose encoding directions are defined by the nodes of an Icosahedral. This scheme was adopted from Diffusion Tensor Imaging (DTI) and is considered an SNR-efficient method when the entire tensor is measured [20].

Schmidt et al. [21] combined the ICOSA6 scheme and multiple data sets with variable velocity sensitivity to increase the dynamic range of the measurement. The RST was found by fitting a 3D Gaussian distribution on all data sets. The results were compared to laser Doppler velocimetry (LDV), the state-of-the-art measurement technique in fluid dynamics for turbulence quantification. After extensive averaging in this in-vitro study, the precise MRI data helped uncover a previously unnoticed source of systematic error: the measurement bias caused by the time derivatives of the velocity field. For example, the acceleration variance, which is inherent to turbulent flow, is interpreted as velocity variance, leading to an overestimation of turbulence. This error locally surpassed 100 % of the reference value in their study, making it the most dominant error source. John et al. [22] addressed this error by reducing encoding times using partial Fourier techniques.

This study develops a sequence less sensitive to fluid acceleration and higher derivatives and demonstrates it in a controlled in vitro environment. The proposed method is demonstrated in the periodic hill setup used by Schmidt et al. [21] to allow for a direct comparison to a state-of-the-art PC MRI method for turbulence quantification. The in-vitro data is extensively averaged to minimize noise and isolate the systematic effects. Based on these results, guidelines are formulated on how a few simple measures can significantly improve future MRI turbulence studies.

2. Material and methods

2.1. Turbulence encoding based on intra-voxel phase dispersion

The fluid motion can be decomposed into a Taylor series in terms of its position r_0, velocity u, acceleration a, and higher derivatives such as the jerk j. The phase angle Φ of the NMR signal depends on these components and the gradient waveform G:

$$\Phi = \Phi_0 + \gamma r_0 \int_{t_0}^{TE} G(t)dt + \gamma u \int_{t_0}^{TE} G(t)tdt + \gamma a \int_{t_0}^{TE} G(t)\frac{t^2}{2}dt + \gamma j \int_{t_0}^{TE} G(t)\frac{t^3}{6}dt + \ldots \quad (1)$$

Where Φ_0 is the initial background phase, t_0 is the isophase point, at which all spins are phase-aligned during excitation, and TE is the echo time. The integral terms in this equation are the gradient moments (M_1, M_2, M_3 …):

$$\Phi = \Phi_0 + \gamma r_0 M_0 + \gamma u M_1 + \frac{\gamma a}{2} M_2 + \frac{\gamma j}{6} M_3 \ldots \quad (2)$$

Within a voxel with inhomogeneous fluid motion, the gradient-induced phases of individual spin ensembles differ and add up incoherently. Assuming an ergodic flow with a Gaussian velocity distribution within the voxel, the signal magnitude $|S|$ becomes a function of the motion-compensated base-line signal $|S_0|$, and the velocity standard deviation σ_u, the acceleration standard deviation σ_a, the jerk standard deviation σ_j, and the standard deviation of higher derivatives [14]:

$$|S| = |S_0| e^{-\frac{\gamma^2}{2}\left(\sigma_u^2\ \Delta M_1^2 + \sigma_a^2 \Delta M_2^2 + \sigma_j^2 \Delta M_3^2 + \ldots\right)} \quad (3)$$

Here, ΔM_1, ΔM_2 and ΔM_3 are the relative gradient moments between the velocity-encoded measurement and the reference measurement, which is typically velocity-compensated. When acceleration and higher derivatives of the velocity field are neglected, this equation becomes the current standard in MRI turbulence quantification [12]:

$$\sigma_u = \sqrt{\frac{2ln(|S|/|S_0|)}{\gamma^2 \Delta M_1^2}} \quad (4)$$

2.2. Assumptions in MRI turbulence quantification

The current method (Eq. (4)) relies on the following assumptions:

(1) The velocity encoding time is much shorter than the integral time scale of the turbulent fluctuations [12,13]
(2) No mean velocity variation within the voxel (as in shear flow) [12]
(3) A Gaussian velocity distribution within the voxel [12]
(4) No variance of the derivatives of velocity, such as acceleration variance, within the voxel

Assumptions (1) to (3) have already been examined by Dillinger et al. [23], Dyverfeldt et al. [12], Veraart et al. [24], and Al-Mubarak et al. [25]. Typically, the time scales in the flow are unknown, and possible errors due to assumption (1) must be tolerated. However, shortening the velocity encoding process minimizes the effect.

Assumption (4) is always inaccurate for turbulent flows. Eq. (5) shows the material derivative of the fluid's velocity $\boldsymbol{u}$.

$$\frac{D\boldsymbol{u}}{Dt} = \frac{\partial \boldsymbol{u}}{\partial t} + \boldsymbol{u} \cdot \nabla \boldsymbol{u} \quad (5)$$

The first term on the right-hand side is the Eulerian derivative of the velocity known as the acceleration. The second term includes the spatial derivative, which results in convective acceleration. If assumption (1) holds, the first term is negligible due to the very short encoding time of

the MRI sequence. Nevertheless, the second term is always non-zero since a turbulent velocity field varies in space. As a result, the spatial velocity gradients inevitably lead to acceleration variance within the voxel. Note that the variance of any higher-order velocity derivatives, such as jerk, is also non-zero in turbulent flow for the same reason.

In Eq. (3), the relative gradient moments $\Delta M_2, \Delta M_3, \ldots$transform these variances in additional signal attenuation, which results in an overestimation of turbulence with the IVPD-technique in Eq. (4). Schmidt et al. [21] mentioned this effect, but otherwise, it belongs to the less-known error sources in MRI turbulence quantification.

Regarding this error due to relative gradient moments, the most accurate results could be obtained with single-point imaging (SPI) methods as they have the shortest possible encoding times resulting in relatively small high-order gradient moments. Also, the second gradient moment M_2 can be controlled straightforwardly with these sequences [26]. However, SPI methods have a relatively long acquisition time.

Radial sequences with center-out trajectories can lead to reduced high-order gradient moments compared to the Cartesian counterpart [27]. However, their practical application is limited due to the 3D non-Cartesian nature of the acquisition requiring long scan times and their sensitivity to gradient delays and other timing inaccuracies as well as modified reconstruction routines.

The state-of-the-art MRI method for velocity and turbulence quantification is currently a Cartesian sequence employing a gradient-recalled echo (GRE). Its drawback is the relatively large high-order gradient moments when acquiring the k-space center, resulting from the prephasing gradient followed by the readout gradient, rendering the signal susceptible to acceleration and higher-order velocity derivatives.

2.3. Velocity-encoded pulse sequence with low sensitivity to the derivatives of turbulence

The objective is to design a Cartesian GRE sequence with reduced high-order relative gradient moments. This decreases the sequence's sensitivity to the variance of the derivatives of velocity, such as the acceleration variance, which can lead to a substantial measurement bias. The determining sequence parameters are the relative gradient moments $\Delta M_2, \Delta M_3, \ldots$ between velocity-encoded and velocity-compensated measurements. Another important parameter is the absolute value of $M_2, M_3, \ldots$ in the velocity-compensated reference scan as these values determine the baseline-magnitude in the IVPD-calculation. A reduction in baseline-magnitude, for example, due to acceleration or jerk-dependent dephasing, reduces SNR and results in less precise turbulence data. In summary, a reduction of $\Delta M_2, \Delta M_3, \ldots$ reduces systematic errors whereas a reduction of $M_2, M_3, \ldots$ in the velocity-compensated reference scan reduces random errors.

These gradient moments vary across the k-space due to the readout and phase encoding gradients. Consequently, instead of controlling the high-order gradient moments, measures are implemented to reduce their overall influence.

Detailed considerations on the sequence design can be found in Appendix A. The main idea is to shorten TE and thus reduce absolute and relative gradient moments. This is achieved through three measures:

- Using the FAST velocity encoding scheme to achieve the shortest gradient design possible with velocity encoding
- Using the highest readout bandwidth possible to shorten the readout gradient and consequently TE
- Using an asymmetric echo, the so-called partial Fourier technique, to minimize the length of both the readout gradient and the prephasing gradient

However, using an asymmetric echo shifts the k-space center to the start of the readout gradient, resulting in a partially measured k-space. Reconstructing this partial echo without any correction results in low-frequency Gibbs ringing in the image [28]. This artifact does not cancel out with the IVPD-technique in Eq. (4), as the ringing differs between the velocity-encoded and reference measurements, thus, resulting in ringing artifacts in the turbulence data. Also, the missing parts of the k-space cannot be inferred from symmetry properties because fluid motion leads to a non-Hermitian k-space [29]. Zero-filling is often used in partial Fourier context, however, as it only interpolates the data and cannot provide further information, it does not influence the ringing.

This study introduces a sequence for turbulence quantification combining the benefits of partial echo imaging with the accuracy of a full echo. Fig. 1 presents the sequence structure. The sequence employs two separately measured partial echoes with opposed readout directions. Each partial echo leads to a k-space of the same dimension as for symmetric echo acquisition, where the center of the k-space is shifted such that the k-space center is located at 1/6 of the full readout direction. Consequently, each asymmetric echo covers 60 % of the whole measured k-space. The resulting overlap between the two echoes within the central k-space region allows to align the datasets and obtain the full k-space.

The specific effects of each of the three applied measures - asymmetric readout, high bandwidth, and velocity encoding - depend on other sequence parameters such as image resolution, maximum velocity encoding value, and system gradient limits. For the sequences executed in the study, the Results section provides numerical values for the changes of $M_2, M_3, \Delta M_2,$ and ΔM_3 to demonstrate the improvements achieved.

2.4. MRI post-processing routine

Matlab 2022b (The Mathworks, Natick, USA) was used for reconstruction and postprocessing.

2.4.1. Alignment of k-space data

Both acquired k-spaces are combined to yield a full k-space before image reconstruction to reduce the ringing induced by the partial echoes. The k-space coordinates of both partial echoes are shifted due to gradient delays and eddy currents, so the partial k-spaces have to be aligned for the positions of both k-space centers to coincide. In this

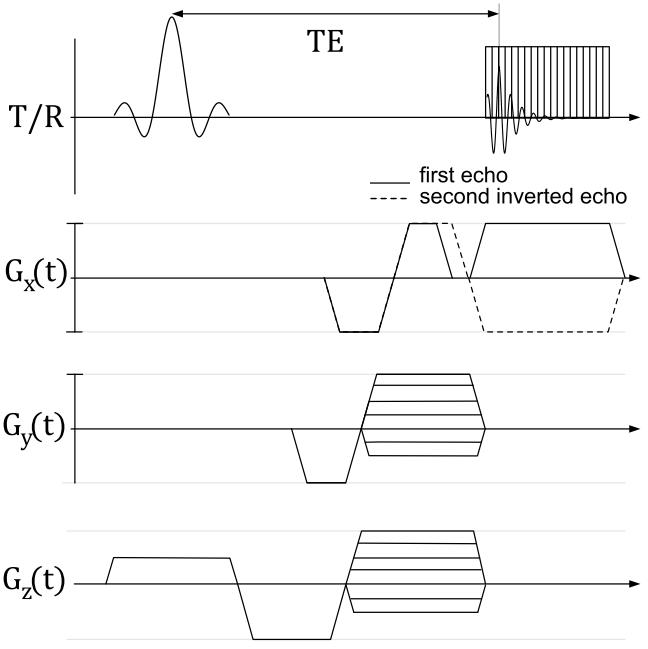


Fig. 1. Sequence structure of the proposed sequence with encoding scheme FAST with the acquisition of the first partial k-space and a second partial k-space using an inverted readout gradient (dotted line).

study, the k-space data is aligned on a subvoxel basis using a linear phase in the image domain. The shift was found according to Block and Uecker [30]. After alignment, the partial k-space data is combined, and overlapping parts are averaged. Fig. 2 illustrates this procedure.

2.4.2. RST reconstruction

The velocity encoding directions are designed using the ICOSA6 encoding scheme to measure the full 6-component RST. The complex images are reconstructed from the multi-channel MRI data using ESPIRiT [31]. Then, the RST is obtained as described in the previous work [21]. With this method, the magnitude data of the ICOSA6 encoded measurements are normalized by the velocity-compensated measurements. Then, a 3D Gaussian distribution is fitted onto the data using a least-squares fit [21]:

$$|S(\boldsymbol{k_u})|/|S_0| = exp\left(-1/2 \cdot \boldsymbol{k_u^T \Sigma^{-1} k_u}\right) \quad (6)$$

whereby $\boldsymbol{k_u} = \gamma\left[\Delta M_{1,x}\ \Delta M_{1,y}\ \Delta M_{1,z}\right]^T$ is the three-component encoding vector and $\boldsymbol{\Sigma}$ is the covariance matrix of the Fourier transform of the 3D Gaussian velocity distribution. The inverse of this matrix ($\boldsymbol{\Sigma^{-1}}$) yields the RST. Moreover, the data points are weighted to reduce the influence of data points with values of $|S(\boldsymbol{k_u})|/|S_0|$ close to zero or one. The highest sensitivity is achieved when the ΔM_1 value results in a 60 % relative signal magnitude. Accordingly, a weighting function is applied which is a Gaussian function centered at $|S(\boldsymbol{k_u})|/|S_0| = 0.6$ with a standard deviation of $|S(\boldsymbol{k_u})|/|S_0| = 0.2$ [12].

2.5. In-vitro experiments

The experiments were conducted in a periodic hill channel depicted in Fig. 3 under identical flow conditions to those described by Schmidt et al. [21]. This test case mirrors the Ercoftac case 81, "Flow over periodic hills" [32,33]. In this setup, the flow separates at the hill crests,

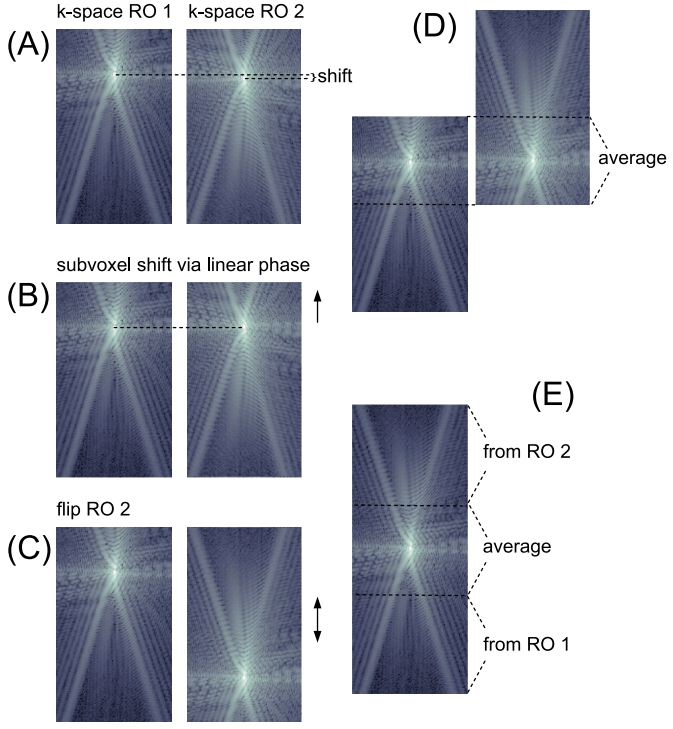


Fig. 2. Combination of the two partial Fourier k-spaces acquired via inverted readout: (A) finding the shift between the two k-space centers via optimization, (B) eliminating the shift by applying a linear phase, flipping the second k-space (C), averaging the overlapping parts of both k-spaces (D) yielding the combined k-space (E).

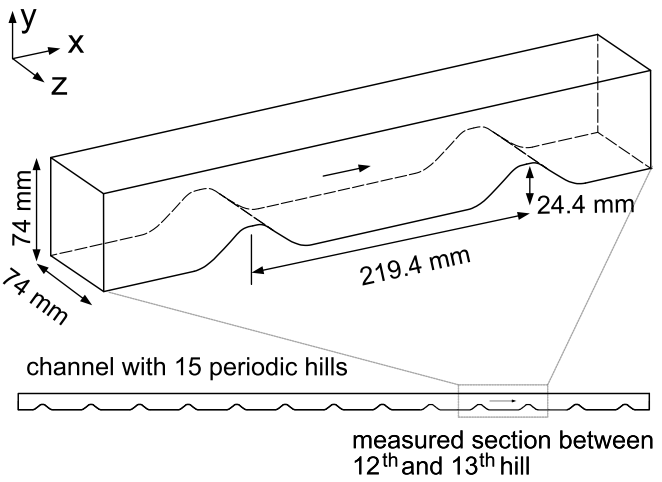


Fig. 3. Schematic of the periodic hill channel.

generating highly non-uniform and anisotropic turbulence, making it a versatile benchmark. LDV data acquired as outlined in Schmidt et al. [21] serves as the ground truth. A FiberFlow system (Dantec dynamics, Skovlunde, Denmark) was used in coincidence mode in a 2-velocity component configuration. At each measurement position, 15,000 to 85,000 valid coincidence samples were measured during 100 s. The measurements were conducted in the symmetry plane of the channel where the traversing system was calibrated to a target placed at a known position. Six lines with a resolution of 0.5 mm and a 2D field with a resolution of 2 mm × 2 mm were measured. The moments of velocity were calculated via BSA Flow Software (Dantec dynamics, Skovlunde, Denmark) applying transit time weighting.

The fluid flow was supplied by two 5.5 kW centrifugal pumps driven by frequency converters and run in parallel. An ultrasound flow rate sensor (Deltawave C-F, Systec Controls, Puchheim, Germany) was used to observe the target flow rate of 255 L/min with a precision of 1 %. The Reynolds number is 29,500 based on the hill height and the axial bulk flow velocity at the hill crests. A 1000 L reservoir, including a thermostat, was added to the flow loop to maintain a constant temperature of 22 °C. The working fluid was purified water with 1 g/L of Copper sulfate added to allow short repetition times and not influence the viscous properties of the fluid. The T1 of this liquid is about 250 ms according to Thangavel and Saritas [34].

The measurements were performed on a 3 T MRI system (Magnetom Tim Trio, Siemens, Germany) with 40 mT/m maximum gradient amplitude and 200 T/m/s maximum gradient slew rate. The FOV, shown in Fig. 3, was placed between the 12th and the 13th of 15 identical consecutive hills. Two receive-only coils with four channels each were

Table 1
Description of the MRI sequence parameters.

Parameter	Value
Matrix size (x,y,z)	(496 mm, 120 mm, 6 mm)
Spatial encoding type (x, y, z)	Frequency, phase, slice
Resolution	1 mm × 1 mm × 6 mm
Echo time	3,9 ms
Repetition time	7 ms
RF flip angle	15°
Receiver bandwidth	920 Hz/pixel
Velocity encoding values (ΔM_1)	[50, 45, 40, 35, 30, 25, 20, 15, 10, 5] mT/m· ms^2
Number of averages	128
Total acquisition time	4 h 11 min
Comments	The k-space is combined from two partial echoes with opposed readout directions, each covering 60 % of the k-space. We call this 10 % echo asymmetry.

placed around the target area from two sides.

The sequence parameters are presented in Table 1. The receiver bandwidth was set to the maximum value. The ΔM_1 values were identical to the previous study with the only exception that the lowest and highest values were omitted since these ΔM_1 were well outside the optimum range for this type of flow. The order of the acquisition loops of the sequence was composed as follows. The first, inner loop consists of the seven encoding directions, i.e. the ICOSA6 directions and one velocity-compensated measurement. The second, third, and fourth loops are the phase encoding, the ΔM_1 encoding, and the averaging loop. 128 averages were acquired to reduce random errors. As the fifth and last loop, the readout was inverted to acquire the two partial k-spaces. This loop was placed at last since a frequent rapid change in the polarity of the readout gradient led to artifacts. As a remedy, a 2-s gap was placed in between the last loop for spoiling. The total measurement matrix amounts to 17,920 2D acquisitions with a total acquisition time of 4 h 11 min.

3. Results

3.1. RST data obtained with the proposed sequence and uncertainty estimation

First, results for the image reconstruction are provided. Fig. 4 shows the data quality achieved with the inverted echo technique compared to individual partial echoes. In part (C), both partial k-spaces are combined for a velocity-compensated measurement using the technique described in Fig. 2. Fig. 4, parts (A) and (B), show the image magnitude computed directly from the individual partial echoes. Compared to the data from the combined echo, the images show blurring at the hill contour and pronounced low-frequent ringing in the readout direction.

Next, the RST reconstruction with the IVPD-technique in Eq. (6) is shown. Fig. 5 illustrates the reconstruction process for two exemplary voxels. The blue-marked voxel is in a highly turbulent flow region, whereas the red-marked voxel is located in a less turbulent region. In part (A) the normalized magnitudes for increasing ΔM_1 values indicate the signal attenuation related to ΔM_1. Part (B) shows the projection of the fitted Gaussian on the encoding direction 3 of the ICOSA6 scheme for both marked voxels. The error bars in the image represent the standard deviation of the magnitude values of all 128 signal averages. Each data point is labeled with its weight used in the fit. The fitted curves are consistent with the data points. Outlier points are in the high-turbulence region (blue) for $\Delta M_1 > 30$ mT/m ms^2. These points, close to the noise floor, lack significant turbulence information and have minimal impact on the fit due to their near-zero weights.

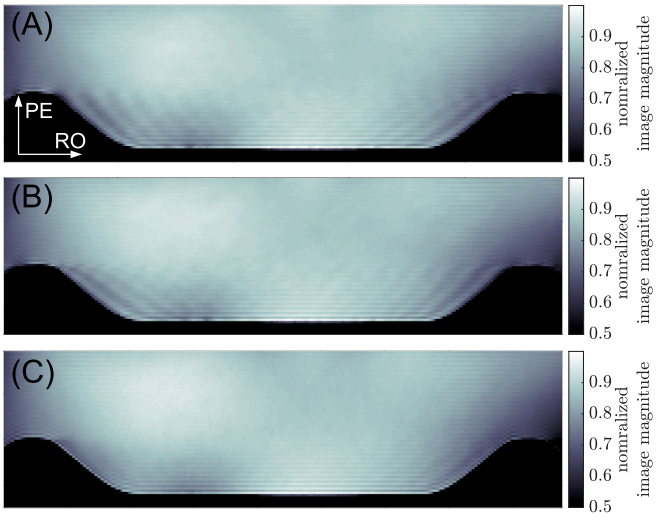


Fig. 4. Normalized image magnitudes from (A) the partial k-space of the first readout, (B) the partial k-space from the second readout, and (C) the combined k-space RO: readout direction, PE: phase encoding direction.

Fig. 6 presents the full measured RST obtained from the combined k-spaces of both readouts. Parts (A) to (C) show the normal stresses whereas parts (D) to (E) depict the shear stresses. The highest stresses can be found in the shear layer behind the hill crest. As a nature of this benchmark case, the RST data exhibit strong non-uniformity and anisotropy. The most dominant component is the normal stress along the streamwise direction, $\overline{u_x' u_x'}$, with a maximum value of about 0.15 m^2/s^2.

The uncertainty in the RST data is calculated using the dual acquisition approach described by Bruschewski et al. [35]. In brief, the RST is reconstructed from two data sets each consisting of half the averages acquired, and the uncertainty is found as the standard deviation between the two calculated RST. For the components shown in Fig. 6, part (A)-(F), the uncertainty values are 0.0013 m^2/s^2, 0.0012 m^2/s^2, 0.0014 m^2/s^2, 0.0010 m^2/s^2, 0.0013 m^2/s^2, 0.0009 m^2/s^2 respectively.

The symmetry of the flow is used to assess the overall degree of experimental error, which includes errors in the boundary conditions of the experiment. The measurements were taken in the symmetry plane, meaning that the shear stress components $\overline{u_x' u_z'}$ and $\overline{u_y' u_z'}$ must be zero everywhere. This is confirmed in Fig. 6 (D) and (E) qualitatively by very low stresses. Quantitatively, the standard deviation and the maximum value in these components are 0.001 m^2/s^2 and 0.012 m^2/s^2. Overall, the uncertainty and error estimates are low when considering the maximum stress value of 0.15 m^2/s^2. Thus, this data set enables a robust assessment of systematic measurement errors.

3.2. Comparison of the results with ground truth and previous data

Fig. 7 provides a straight comparison of the MRI data obtained in this study, the LDV data representing the ground truth, and the MRI data obtained with a conventional PC MRI technique in Schmidt et al. [21]. All data sets were measured under identical flow conditions. The new MRI data is more consistent with the LDV data compared to the results in the previous study.

Fig. 8 provides a more quantitative comparison of the three data sets. Line plots of the LDV data and both MRI data sets acquired using the conventional and the new sequence are shown at multiple streamwise locations for all RST components for which LDV data were available: $\overline{u_x' u_x'}$, $\overline{u_y' u_y'}$ and $\overline{u_x' u_y'}$. Rows (B) and (D) display the components dependent on the readout direction x. The new MRI data exhibit substantially lower deviations from the LDV data compared to the previous results. The new sequence reduces the maximum deviation from 0.05 m^2/s^2 to approximately 0.01 m^2/s^2 for both normal and shear stresses. The relative error at maximal deviation decreases from 45 % to 7 % for the normal stresses and from 110 % to 17 % for the shear stresses. Fig. 8, row (C), shows smaller differences between the two MRI results and, overall, a low deviation compared to LDV. This RST component corresponds to the normal stress in the phase encoding direction y.

3.3. Calculation of gradient moments

The Appendix B Tables (B.1) and (B.2) provide the absolute and relative gradient moments M_2, ΔM_2, M_3 and ΔM_3 in the k-space center for the highest common ΔM_1 of 50 mT/m· ms^2 of the two MRI sequences compared in the previous section. They were calculated using Eqs. (A.1) and (A.2) from Appendix A. Generally, the gradient moments vary with spatial direction and the ICOSA6 encoding direction. The changes are here represented by the magnitude of the gradient moments, defined as the root-sum-squared value of the spatial components of the gradient moments.

The absolute values of M_2 and M_3 in the velocity-compensated reference scan affect the SNR of the baseline signal and, therefore, the precision of the RST data. The proposed sequence has reduced the

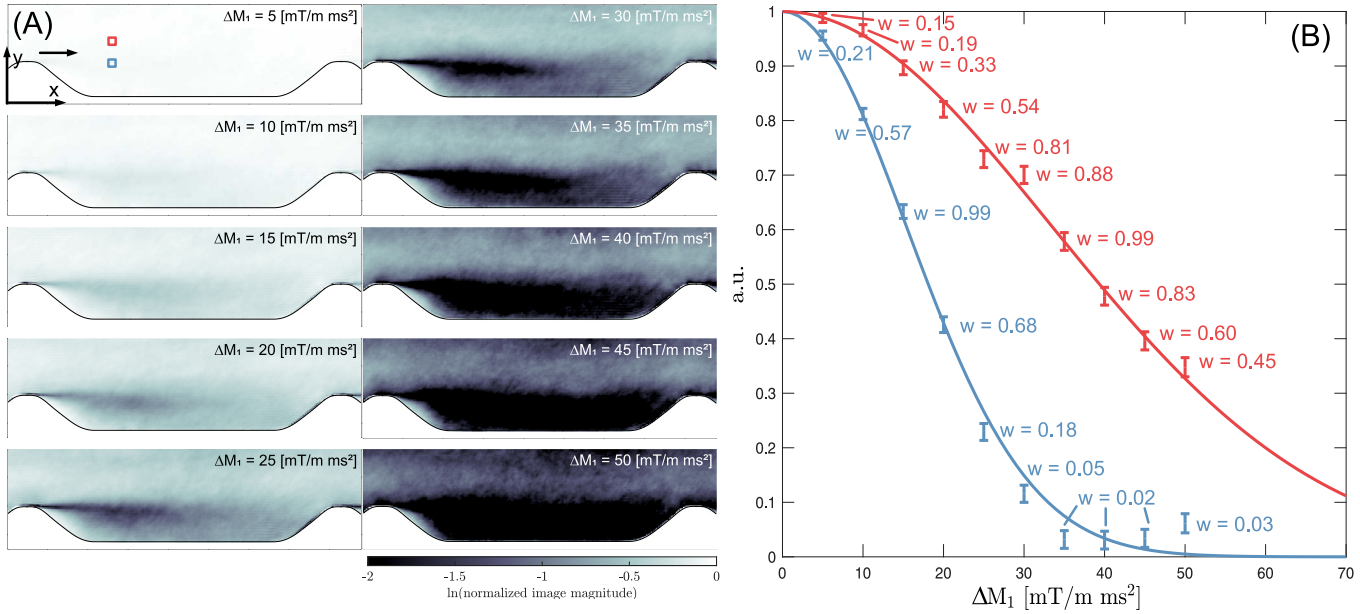


Fig. 5. IVPD reconstruction for two exemplary voxels marked red and blue. (A): normalized magnitude images $|S(k_u)|/|S_0|$ for encoding direction 3 of the ICOSA6 scheme for increasing ΔM_1, flow direction indicated by the arrow. (B): Projection of 3D Gaussian fit to encoding direction 3 of the ICOSA6 scheme for two exemplary voxels marked red and blue in (A), the data with one standard deviation from all 128 measurements is depicted as errorbars labeled with the weight used in the fit. (For interpretation of the references to colour in this figure legend, the reader is referred to the web version of this article.)

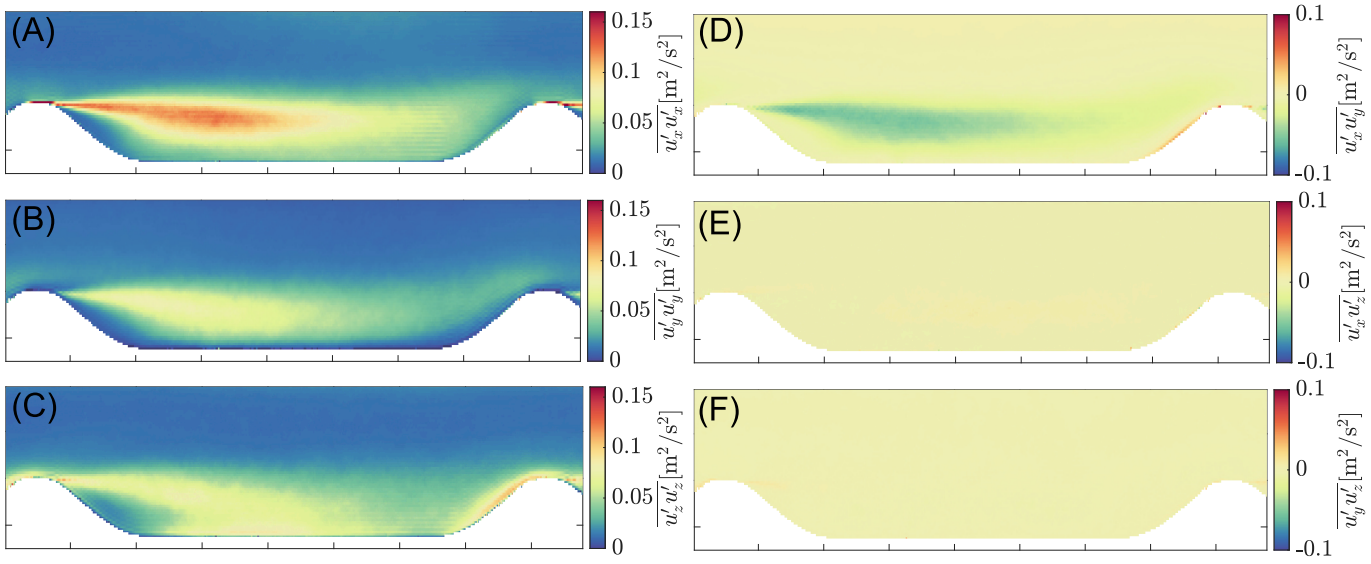


Fig. 6. Full measured RST reconstructed from combined k-spaces, normal stresses (A)-(C), shear stresses (D)-(F).

magnitude of M_2 and M_3 by 94 % and 98 %.

On average, the proposed sequence has reduced the magnitude of the relative gradient moments ΔM_2 and ΔM_3 by 32 % and 56 %. For the fourth encoding direction the magnitude value of ΔM_2 and ΔM_3 are reduced even more by 39 % and 67 %. This encoding direction contributes mainly to the RST components $\overline{u'_x u_{x'}}$ and $\overline{u'_x u_{y'}}$, where the strongest improvements are evident in (Fig. 8). Additionally, ΔM_2 and ΔM_3 are more uniformly distributed over all spatial and encoding directions than in the sequence from the previous study. Therefore, measurement errors caused by the variance of acceleration and jerk appear more isotropic in the results compared to the previous sequence.

4. Discussion

The objective was to investigate and reduce systematic errors in state-of-the-art MRI methods for turbulence quantification. In-vitro experiments were carried out within a controlled environment, yielding data nearly devoid of noise which was compared to a known ground truth.

The proposed sequence was designed to reduce the influence of the variance of the derivatives of velocity, such as the acceleration variance, which can lead to a substantial measurement bias in turbulence quantification. The objective was to reduce the relative gradient moments ΔM_2, ΔM_3, … between velocity-encoded and velocity-compensated measurements and the absolute value of M_2, M_3, … in the velocity-compensated measurement.

Figs. 7 and 8 illustrate the good agreement between the MRI data

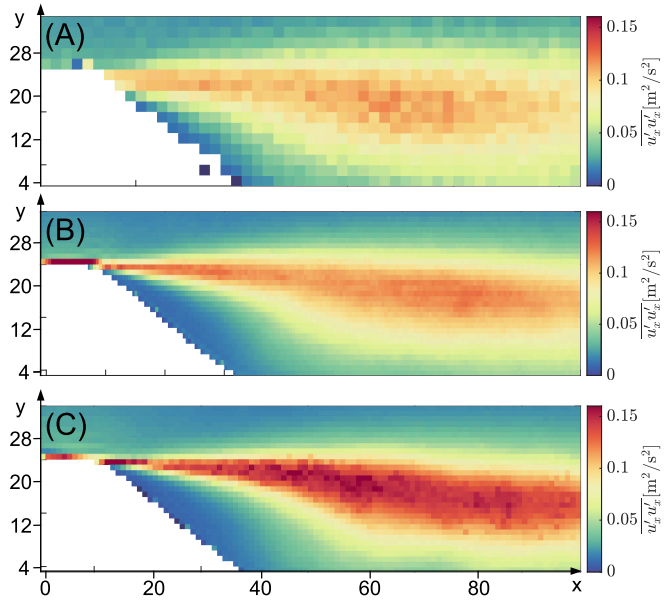


Fig. 7. The first component of the RST obtained using LDV (A), with the proposed sequence (two partial k-spaces acquired with inverted read-out gradients and combination to a full k-space) (B) and with a cartesian sequence with symmetrical readout from the study of Schmidt et al. [21] (C).

acquired with the proposed sequence and the reference LDV data. Compared to a previous study with a conventional PC MRI sequence, the maximum degree of error was reduced 5-fold. The strongest improvements were achieved for the RST components that depend on the readout direction. The changes in the RST component dependent on the phase-encoding direction were less pronounced since the error in the data from the previous study was already low.

When comparing the numerical values for the gradient moments with the achieved improvements, it is evident that the theoretical predictions align perfectly with the practical results. The accuracy of MRI turbulence quantification strongly correlates with the reduction of high-order gradient moments.

The improvements were achieved through three measures: applying FAST velocity encoding, maximizing readout bandwidth, and using an asymmetric readout. To reduce the ringing artifacts induced by the asymmetric k-space, a second inverted readout was utilized, and both partial k-spaces were combined into a complete k-space. Fig. 4 (A) shows substantially less ringing in the magnitude image when the combined k-space is used, compared to Fig. 4 (B) and (C), where only the partial k-spaces are considered. Ringing artifacts in the RST data are almost entirely removed.

The following recommendations are derived from these findings:

- FAST velocity encoding, high receiver bandwidth, and an asymmetric echo are effective methods to reduce the higher-order gradient moments of the sequence, thereby decreasing its sensitivity to the variance of velocity derivatives, such as acceleration

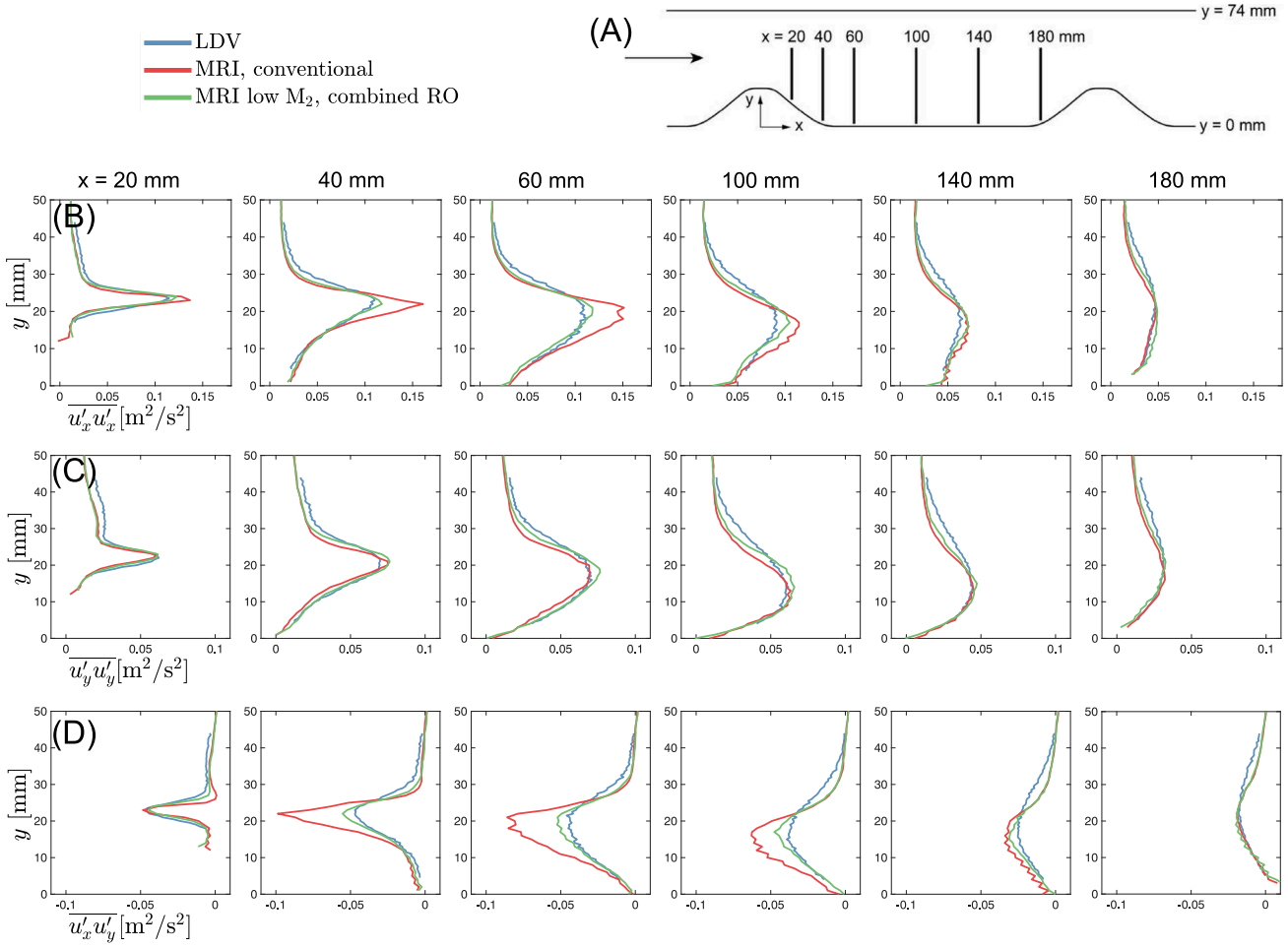


Fig. 8. RST components at locations indicated in (A) were acquired using LDV (blue), with a conventional sequence (red), and with the proposed sequence (green). (For interpretation of the references to colour in this figure legend, the reader is referred to the web version of this article.)

variance, which can otherwise lead to an overestimation of turbulence.
- It is recommended to acquire a second inverted echo and combine both partial echoes to reduce imaging artifacts and achieve the accuracy of a full k-space.

In this in-vitro study, data were extensively averaged, and multiple encoding values were employed to minimize noise and isolate systematic effects. For in-vivo studies, image noise will partially obscure these errors but these systematic effects will nonetheless remain present.

When applying the proposed recommendations to standard techniques in medical contexts, the acquisition time nearly doubles, as the new method relies on acquiring two partial echoes. However, this limitation could be mitigated using advanced acceleration techniques such as parallel imaging or sparse sampling strategies. Importantly, RST fields typically exhibit smoother spatial variations and fewer details compared to velocity fields. As a result, compressed sensing stands out as a promising approach to significantly reduce acquisition times while maintaining measurement accuracy.

5. Conclusion

MRI turbulence quantification relies on several assumptions that can lead to significant measurement errors. This study demonstrated that conventional PC MRI methods using the IVPD reconstruction technique are particularly sensitive to the variance of the velocity field derivatives, such as acceleration variance, which are inherent in turbulent flows. To address these issues, several measures were proposed and implemented, resulting in a 5-fold reduction in measurement errors in an in-vitro experiment.

Future research should focus on in-vivo validation and the development of acceleration techniques to reduce imaging times to clinically practical levels.

CRediT authorship contribution statement

Swantje Romig: Writing – original draft, Visualization, Software, Methodology, Investigation, Data curation. **Kristine John:** Writing – review & editing, Software, Methodology, Conceptualization. **Simon Schmidt:** Writing – review & editing, Software, Methodology, Conceptualization. **Sebastian Schmitter:** Writing – review & editing, Methodology, Conceptualization. **Sven Grundmann:** Writing – review & editing, Resources, Funding acquisition. **Martin Bruschewski:** Writing – review & editing, Supervision, Project administration, Methodology, Investigation, Funding acquisition, Conceptualization.

Acknowledgements

This work was funded by the German Federal Ministry for Economic Affairs and Climate Action under grant number 20E2229 on the basis of the decision by the German Bundestag.

Funded by the Deutsche Forschungsgemeinschaft (DFG, German Research Foundation) - INST 264/222-1.

Appendix A. Sequence design for reduced higher-order absolute and relative gradient moments

The n^{th} gradient moment of each gradient lobe can be calculated based on its zeroth Moment M_o, the starting time t_G relative to the time of excitation, and the length of the gradient T_G : [36]

$$M_n = M_0(t_G + T_G/2\,)^n \tag{A.1}$$

Assuming that the timing of the gradients in the velocity-sensitive measurement and the velocity-compensated reference measurement is similar, the same approximations can be made for the n^{th} relative gradient moment:

$$\Delta M_n = \Delta M_0(t_G + T_G/2\,)^n \tag{A.2}$$

From these equations, it can be concluded that the most effective way to reduce absolute and relative high-order gradient moments is by shortening the duration of all gradients (minimize T_G) and positioning them as close as possible to the time of excitation (minimize t_G), resulting in a shorter TE.

Velocity-encoded GRE methods typically use one of two velocity encoding schemes: the FAST scheme [37] or the ECHO scheme [38]. Compared to the FAST encoding scheme, the ECHO scheme reduces displacement artifacts but requires a longer gradient duration and the overall gradient area is larger for the phase encoding direction [39]. Consequently, the FAST scheme emerges more favorable for reducing higher-order gradient moments. Reduced duration of the gradients on the phase encoding axis can lead to shorter delays on both the frequency and slice axes.

Regarding spatial encoding, improvements can be made with the gradients in the readout direction. The readout bandwidth can be adjusted independently of any other gradient. A higher bandwidth results in a shorter readout gradient duration, reducing the high-order moments of this gradient. Next, the prephasing gradient, executed before the readout gradient, is modified. Depending on how the prephasing gradient is combined with the velocity encoding gradients, a shorter prephasing gradient can reduce higher-order moments of both the prephasing and readout gradients. A shorter prephasing gradient reduces TE such that the high-order gradient moments in the phase encoding direction are also reduced since dead times in this gradient direction are decreased allowing earlier gradient execution.

A reduction of the prephasing gradient can also be achieved using an asymmetric echo because the area of the readout gradient that needs to be compensated by the prephasing gradient before the echo center is smaller.

Appendix B. Absolute and relative gradient moments for the used sequences

Table B.1

M_2 and ΔM_2 in $\frac{mT}{m}ms^3$ for the proposed sequence and for the sequence used in the previous study [21] calculated using Eqs. (A.1) and (A.2).

Coordinate direction →	x	y	z	x	y	z
Encoding direction ↓	Proposed sequence			Sequence from the previous study		
M_2						
ref	1.09	0	4.247	35.4	0	65.7
RMS = $\sqrt{M_{2_x}^2 + M_{2_y}^2 + M_{2_z}^2}$		4.38			74.63	
1	−117	0	203	−121	0	371
2	−117	0	−138	−121	0	−102
3	−166	124	0	−198	169	0
4	202	124	0	380	169	0
5	0	176	113	0	258	243
6	0	−176	113	0	−258	243
ΔM_2						
1-ref	−118	0	198	−156	0	305
2-ref	−118	0	−143	−156	0	−167
3-ref	−167	124	0	−233	169	0
4-ref	200	124	0	345	169	0
5-ref	0	176	109	0	258	178
6-ref	0	−176	109	0	−258	178
RMS = $\sqrt{\sum_{i=\{x,y,z\}}\sum_j \Delta M_{2_{ij-ref}}^2}$		521.40			772.35	

Table B.2

M_3 and ΔM_3 in $\frac{mT}{m}ms^4$ for the proposed sequence and for the sequence used in the previous study [21] calculated using Eqs. (A.1) and (A.2).

Coordinate direction →	x	y	z	x	y	z
Encoding direction ↓	Proposed sequence			Sequence from the previous study		
M_3						
ref	11.6	0	11.1	516	0	361
RMS = $\sqrt{M_{3_x}^2 + M_{3_y}^2 + M_{3_z}^2}$		16.06			629.74	
1	−381	0	731	−125	0	2080
2	−381	0	−361	−125	0	−198
3	−481	437	0	−364	816	0
4	754	437	0	2620	816	0
5	0	550	359	0	1190	1300
6	0	−550	359	0	−1190	1300
ΔM_3						
1-ref	−393	0	731	−641	0	1715
2-ref	−393	0	−361	−641	0	−559
3-ref	−492	437	111	−880	816	0
4-ref	742	437	111	2110	816	0
5-ref	0	550	359	0	1190	944
6-ref	0	−550	359	0	−1190	944
RMS = $\sqrt{\sum_{i=\{x,y,z\}}\sum_j \Delta M_{3_{ij-ref}}^2}$		1719.45			3904.88	

References

[1] Riva A, Eriksson J, Viola F, Strula F, Votta E, Ebbers T, et al. Impact of dobutamine stress on diastolic energetic efficiency of healthy left ventricle: an in vivo kinetic energy analysis. Front Cardiovac Med 2023;10:1103751. https://doi.org/10.3389/fcvm.2023.1103751.

[2] Dyverfeldt P, Trenti C, Ziegler M, Bjarnegård N, Lindenberger M. Helical flow in tortuous aortas and its relationship to turbulence: a whole-aorta 4D flow MRI study. Front Cardiovasc Med 2023;10:1124604. https://doi.org/10.3389/fcvm.2023.1124604.

[3] Walheim J, Dillinger H, Gotschy A, Kozerke S. 5D flow tensor MRI to efficiently map Reynolds stresses of aortic blood flow in-vivo. Sci Rep 2019;9(1):18794. https://doi.org/10.1038/s41598-019-55353-x.

[4] Vishnevskiy V, Dillinger H, Walheim J, Zhang L, Kozerke S. Improved in vivo estimation of the reynolds stress tensor from 4D und 5D flow MRI using Cholesky decomposition-based neural networks. In: Proc Intl Soc Mag Reson Med. 28; 2020.

[5] Ha H, Huh HK, Park KJ, et al. In-vitro and in-vivo assessment of 4D flow MRI Reynolds stress mapping for pulsatile blood flow. Front Bioeng Biotechnol 2021;9:774954. https://doi.org/10.3389/fbioe.2021.774954.

[6] Dong H, Im C, Kang C, Cho JH, Jang I, Song S. Investigation of flow behavior in a refrigerator machine room using magnetic resonance velocimetry. Int J Heat Mass Transf 2023;214:124446. https://doi.org/10.1016/j.ijheatmasstransfer.2023.124446.

[7] Elgersma SV, Sederman AJ, Mantle MD, Guédon CM, Wells GJ, Gladden LF. Magnetic resonance velocity imaging of turbulent gas flow in a packed bed catalyst support beds. Chem Eng J 2023;475:145445. https://doi.org/10.1016/j.cej.2023.145445.

[8] Clarke D, Galvosas P, Holland D. Characterization of unsteady flow in a 3D-printed Schwarz diamond monolith using magnetic resonance velocimetry. AICHE J 2023;69(8):e18097. https://doi.org/10.1002/aic.18097.

[9] Moran PR. A flow velocity zeugmatographic interlace for NMR imaging in humans. Magn Reson Imaging 1982;1(4):197–203. https://doi.org/10.1016/0730-725X(82)90170-9.

[10] Callaghan PT, Eccles CD, Xia Y. NMR microscopy of dynamic displacements: k-space and q-space imaging. J Phys E Sci Instrum 1988;21(8):820–2. https://doi.org/10.1088/0022-3735/21/8/017.

[11] Newling B, Piorier CC, Zhi Y, Rioux JA, Coristine AJ, Roach D, et al. Velocity imaging of highly turbulent gas flow. Phys Rev Lett 2004;93(15):154503. https://doi.org/10.1103/PhysRevLett.93.154503.

[12] Dyverfeldt P, Gårdhagen R, Sigfridsson A, Karlsson M, Ebbers T. On MRI turbulence quantification. Magn Reson Imaging 2009;27(7):913–22. https://doi.org/10.1016/j.mri.2009.05.004.
[13] Gao JH, Gore JC. Turbulent flow effects on NMR imaging: measurement of turbulent intensity. Med Phys 1991;18(5):1045–51. https://doi.org/10.1118/1.596645.
[14] Dyverfeldt P, Sigfridsson A, Kvitting JPE, Ebbers T. Quantification of intravoxel velocity standard deviation and turbulence intensity by generalizing phase-contrast MRI. Magn Reson Med 2006;56(4):850–8. https://doi.org/10.1002/mrm.21022.
[15] Ha H, Kvitting JPE, Dyverfeldt P, Ebbers T. 4D flow MRI quantification of blood flow patterns, turbulence and pressure drop in normal and stenotic prosthetic heart valves. Magn Reson Imaging 2019;55:118–27. https://doi.org/10.1016/j.mri.2018.09.024.
[16] Binter C, Knobloch V, Manka R, Sigfridsson A, Kozerke S. Bayesian multipoint velocity encoding for concurrent flow and turbulence mapping. Magn Reson Med 2012;69(5):1337–45. https://doi.org/10.1002/mrm.24370.
[17] Knobloch V, Binter C, Gülan U, Sigfridaaon A, Holzner M, Beat Lüthi, et al. Mapping mean and fluctuating velocities by Bayesian multipoint MR velocity encoding-validation against 3D particle tracking velocimetry. Magn Reson Med 2014;71(4):1405–15. https://doi.org/10.1002/mrm.24785.
[18] Elkins CJ, Alley MT, Saetran L, Eaton JK. Three-dimensional magnetic resonance velocimetry measurements of turbulence quantities in complex flow. Exp Fluids 2009;46(2):285–96. https://doi.org/10.1007/s00348-008-0559-4.
[19] Haraldsson H, Kefayati S, Ahn S, Dyverfeldt P, Lantz J, Karlsson M, et al. Assessment of Reynolds stress components and turbulent pressure loss using 4D flow MRI with extended motion encoding. Magn Reson Med 2018;79(4):1962–71. https://doi.org/10.1002/mrm.26853.
[20] Hasan KM, Parker DL, Alexander AL. Comparison of gradient encoding schemes for diffusion-tensor MRI. J Magn Reson Imaging 2001;13(5):769–80. https://doi.org/10.1002/jmri.1107.
[21] Schmidt S, John K, Kim SJ, Flassbeck S, Schmitter S, Bruschewski M. Reynolds stress tensor measurements using magnetic resonance velocimetry: expansion of the dynamic measurement range and analysis of systematic measurement errors. Exp Fluids 2021;62(6):121. https://doi.org/10.1007/s00348-021-03218-3.
[22] John K, Romig S, Rehm M, Hadžić H, Pohl P, Grundmann S, Bruschewski M. Volumetric measurements of mean velocity vector and reynolds stress tensor for CFD validation: Magnetic resonance velocimetry in a nuclear fuel assembly model with mixing grids. Flow Turbul Combust 2024. https://doi.org/10.1007/s10494-025-00636-9.
[23] Dillinger H, McGrath C, Guenthner C, Kozerke S. Fundamentals of turbulent flow spectrum imaging. Magn Reson Med 2022;87(3):1231–49. https://doi.org/10.1002/mrm.29001.
[24] Veraart J, Poot DHJ, van Hecke T, Blockx I, Van der Linden A, Verhoye M, et al. More accurate estimation of diffusion tensor parameters using diffusion Kurtosis imaging. Magn Reson Med 2011;65(1):138–45. https://doi.org/10.1002/mrm.22603.
[25] Al-Mubarak HF, Vallatos A, M. HW. Impact of turbulence-induced asymmetric propagators on the accuracy of phase-contrast velocimetry. J Magn Reson 2021;325:106929. https://doi.org/10.1016/j.jmr.2021.106929.
[26] Schmidt S, Bruschewski M, Flassbeck S, John K, Grundmann S, Ladd ME, et al. Phase-contrast acceleration mapping with synchronized encoding. Magn Reson Med 2021;86(6):3201–10. https://doi.org/10.1002/mrm.28948.
[27] Degenhardt K, Schmidt S, Aigner CS, Kratzer FJ, Seiter DP, Mueller M, et al. Toward accurate and fast velocity quantification with 3D ultrashort TE phase-contrast imaging. Magn Reson Med 2024:1–16. https://doi.org/10.1002/mrm.29978.
[28] Lee HH, Novikov DS, Fieremans E. Removal of partial Fourier-induced Gibbs (RPG) ringing artifacts in MRI. Magn Reson Med 2021;86(5):2733–50. https://doi.org/10.1002/mrm.28830.
[29] MacFall JR, Pelc NJ, Vavrek RM. Correction of spatially dependent phase shifts for partial Fourier imaging. Magn Reson Imaging 1988;6(2):143–55. https://doi.org/10.1016/0730-725X(88)90444-4.
[30] Block K, Uecker M. Simple method for adaptive gradient-delay compensation in radial MRI. In: Proc Intl Soc Mag Reson Med. 19; 2011.
[31] Uecker M, Lai P, Murphy MJ, Virtue P, Elad M, Pauly JM, et al. ESPIRiT—an eigenvalue approach to autocalibrating parallel MRI: where SENSE meets GRAPPA. Magn Reson Med 2014;71(3):990–1001. https://doi.org/10.1002/mrm.24751.
[32] Temmerman L, Leschziner MA. Large eddy simulation of separated flow in a streamwise periodic channel constriction. In: Second Symp Turbul Shear Flow Phenom; 2001.
[33] Jang YJ, Leschziner MA, Abe K, Temmerman L. Investigation of anisotropy-resolving turbulence models by reference to highly-resolved LES data for separated flow. Flow Turbul Combust 2002;69:161–203. https://doi.org/10.1023/A:1024764307706.
[34] Thangavel K, Saritas EÜ. Aqueous paramagnetic solutions for MRI phantoms at 3 T: a detailed study on relaxivities. Turk J Electr Eng Comput Sci 2017;25(3):2108–21. https://doi.org/10.3906/elk-1602-123.
[35] Bruschewski M, Freudenhammer D, Buchenberg WB, Schiffer HP, Grundmann S. Estimation of measurement uncertainty in magnetic resonance velocimetry based on statistical models. Exp Fluids 2016;57:1–13. https://doi.org/10.1007/s00348-016-2163-3.
[36] Simonetti OP, Wendt RE, Duerk JL. Significance of the point of expansion in interpretation of gradient moments and motion sensitivity. J Magn Reson Imaging 1991;1(5):569–77. https://doi.org/10.1002/jmri.1880010510.
[37] Bernstein MA, Shimakawa A, Pelc NJ. Minimizing TE in moment-nulled or flow-encoded two-and three-dimensional gradient-echo imaging. J Magn Reson Imaging 1992;5:583–8. https://doi.org/10.1002/jmri.1880020517.
[38] Nishimura DG, Jackson JI, Pauly JM. On the nature and reduction of displacement artifact in flow images. Magn Reson Med 1991;6(2):481–92. https://doi.org/10.1016/0730-725x(88)90444-4.
[39] Schmidt S, Flassbeck S, Bachert P, Ladd ME, Schmitter S. Velocity encoding and velocity compensation for multi-spoke RF excitation. Magn Reson Imaging 2020;66:69–85. https://doi.org/10.1016/j.mri.2019.11.007.